

Unravelling the mechanism of the semiconducting-like behavior and its relation to superconductivity in $(\text{CaFe}_{1-x}\text{Pt}_x\text{As})_{10}\text{Pt}_3\text{As}_8$

Run Yang,^{1,2,3} Yaomin Dai,⁴ Jia Yu,^{1,3} Qiangtao Sui,^{1,3} Yongqing Cai,^{1,3} Zhian Ren,^{1,3,5} Jungseek Hwang,^{2,6} Hong Xiao,⁷ Xingjiang Zhou,^{1,3,5} Xianggang Qiu,^{1,3,5,*} and Christopher C. Homes^{2,†}

¹*Beijing National Laboratory for Condensed Matter Physics,
Institute of Physics, Chinese Academy of Sciences, Beijing 100190, China*

²*Condensed Matter Physics and Materials Science Division,
Brookhaven National Laboratory, Upton, New York 11973, USA*

³*School of Physical Sciences, University of Chinese Academy of Sciences, Beijing 100049, China*

⁴*Center for Superconducting Physics and Materials,
National Laboratory of Solid State Microstructures and Department of Physics, Nanjing University, Nanjing 210093, China*

⁵*Collaborative Innovation Center of Quantum Matter, Beijing 100084, China*

⁶*Department of Physics, Sungkyunkwan University, Suwon, Gyeonggi-do 16419, Korea*

⁷*Center for High Pressure Science and Technology Advanced Research, Beijing 100094, China*

(Dated: January 26, 2022; version 6)

The temperature-dependence of the in-plane optical properties of $(\text{CaFe}_{1-x}\text{Pt}_x\text{As})_{10}\text{Pt}_3\text{As}_8$ have been investigated for the undoped ($x = 0$) parent compound, and the optimally-doped ($x = 0.1$) superconducting material ($T_c \simeq 12$ K) over a wide frequency range. The optical conductivity has been described using two free-carrier (Drude) components, in combination with oscillators to describe interband transitions. At room temperature, the parent compound may be described by a strong, broad Drude term, as well as a narrow, weaker Drude component. Below the structural and magnetic transitions at $\simeq 96$ and 83 K, respectively, strength is transferred from the free-carrier components into a bound excitation at $\simeq 1000$ cm^{-1} , and the material exhibits semiconducting-like behavior. In the optimally-doped sample, at room temperature the optical properties are again described by narrow and broad Drude responses comparable to the parent compound; however, below $T^* \simeq 100$ K, strength from the narrow Drude is transferred into a newly-emergent low-energy peak at $\simeq 120$ cm^{-1} , which arises from a localization process, resulting in semiconducting-like behavior. Interestingly, below T_c , this peak also contributes to the superfluid weight, indicating that some localized electrons condense into Cooper pairs; this observation may provide insight into the pairing mechanism in iron-based superconductors.

PACS numbers: 72.15.-v, 74.70.-b, 78.30.-j

I. INTRODUCTION

The discovery of iron-based superconductors has prompted in an intensive investigation of this class of materials in the hope of discovering new compounds with high superconducting critical temperatures (T_c 's) [1–3]. In both iron-based superconductors (FeSCs) and cuprates, a variety of unusual normal-state phenomena are observed that are believed to have an important connection to the superconductivity (SC) [4, 5]. In the optimally-doped cuprates the resistivity often shows a peculiar non-saturating linear temperature dependence that at high temperature may violate the Mott-Ioffe-Regel limit [6], leading it to be described as a marginal Fermi liquid [7]. A pseudogap develops in underdoped regime well above the critical temperature (T_c) [8], which has been interpreted as evidence for preformed Cooper pairs without global phase coherence [9–11]; on the other hand, competing orders, such as charge-ordered states, have also been proposed as the origin of this feature [12].

In FeSCs, one of the most interesting phenomena in the normal state is the emergence of nematicity, or rotational symmetry breaking of the electronic states [13]; however, its origin and relation to the superconductivity in these materials is still uncertain [5].

The $(\text{CaFe}_{1-x}\text{Pt}_x\text{As})_{10}\text{Pt}_3\text{As}_8$ (Ca 10-3-8) materials exhibit some rather interesting properties. The unit cell of the undoped parent compound is shown in Fig. 1(a); the conducting Fe–As layers are separated by Ca atoms and insulating Pt_3As_8 layers, resulting in an inter-layer distance as large as 10.6 Å. Transport measurements indicate this material is highly two dimensional (2D) [14]. The phase diagram [Fig. 4(a) of Ref. 15] indicates that the parent compound is an antiferromagnetic (AFM) semiconductor; the resistivity and other experimental probes [16–19] indicate that this material undergoes structural and magnetic transitions at $T_s \simeq 96$ K and $T_N \simeq 83$ K, respectively. Through the application of pressure, or by doping Pt on the Fe site (electron doping), the AFM order is suppressed, and superconductivity emerges with a maximum $T_c \simeq 12$ K in the optimally-doped material [20]. However, the semiconducting-like behavior still remains (resistivity increases upon cooling) above the AFM and SC dome [14, 15], which is reminiscent of the pseudogap-like behavior in cuprates [9]. In-

* xgqiu@iphy.ac.cn

† homes@bnl.gov

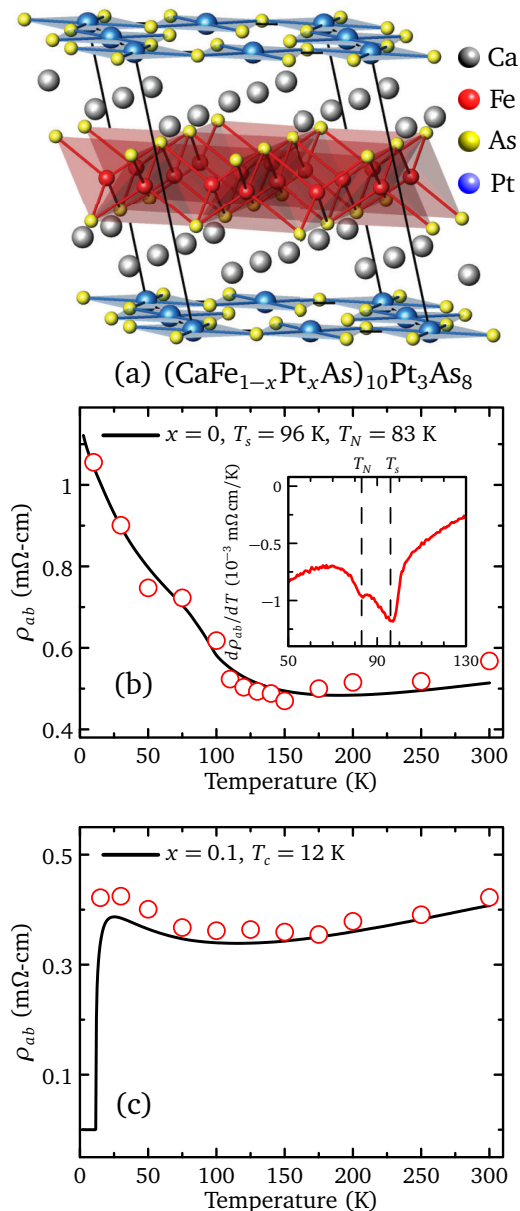


Figure 1. (a) The triclinic unit cell of $(\text{CaFe}_{1-x}\text{Pt}_x\text{As})_{10}\text{Pt}_3\text{As}_8$ showing the Fe–As layers separated by Ca and Pt_3As_8 sheets. (b) The in-plane resistivity of the $x = 0$ (undoped) sample showing a semiconducting-like response at low temperature. Inset: $d\rho_{ab}/dT$ showing local minima at T_s and T_N . (c) The resistivity for the $x = 0.1$ (optimally-doped) sample, again showing a semiconducting response just above T_c . The circles denoting $\sigma_1(\omega \rightarrow 0) \equiv \sigma_{dc}$ are in good agreement with the transport data.

investigating the origin of such distinct behavior and how it evolves into a superconductor may provide insight into the pairing mechanism in iron-based superconductors.

In this work the temperature dependence of the in-plane optical properties of $(\text{CaFe}_{1-x}\text{Pt}_x\text{As})_{10}\text{Pt}_3\text{As}_8$ for undoped ($x = 0$) and optimally-doped ($x = 0.1$) samples is investigated. The real part of the optical conductivity

is particularly useful as it yields information about the free-carrier response and interband transitions; in the zero-frequency limit, the dc conductivity is recovered, allowing comparisons to be made with transport data. The optical properties suggest that the semiconducting-like behavior in the parent compound likely originates from AFM order that leads to a reconstruction of the Fermi surface and a decrease in the carrier concentration. In the optimally-doped sample, torque magnetometry indicates superconducting fluctuations well above T_c , suggesting that this material may not be homogeneous. Along with the semiconducting-like behavior, at low temperature we observe the emergence of a peak in the optical conductivity in the far-infrared region, which is attributed to localization driven by either scattering from impurities or AFM spin fluctuations. Interestingly, below T_c , this peak also contributes to the superfluid weight, indicating that there is likely a relationship between magnetism and superconductivity.

II. EXPERIMENT

High-quality single crystals of $(\text{CaFe}_{1-x}\text{Pt}_x\text{As})_{10}\text{Pt}_3\text{As}_8$ with good cleavage planes (001) were synthesized using self-flux method [21]. The temperature dependence of the in-plane resistivity for the undoped and optimally-doped materials is shown in Figs. 1(b) and 1(c), respectively. At room temperature, the resistivity of both materials is comparable. In the undoped material, ρ_{ab} exhibits relatively little temperature dependence until ≈ 150 K, below which it exhibits a semiconducting response, increasing gradually, with inflection points at $T_N \approx 83$ and $T_s \approx 96$ K, shown in the inset of Fig. 1(b). The resistivity of the doped material initially decreases as the temperature is reduced and then undergoes a slight upturn resulting in a broad minimum at about 100 K; below $T_c \approx 12$ K the resistivity abruptly drops to zero. The reflectance from freshly-cleaved surfaces has been measured over a wide temperature (~ 5 to 300 K) and frequency range (~ 2 meV to about 5 eV) at a near-normal angle of incidence for light polarized in the a - b planes using an *in situ* evaporation technique [22]. The complex optical properties have been determined from a Kramers-Kronig analysis of the reflectivity. The reflectivity is shown in Supplementary Figs. S1(a) and S1(b); the details of the Kramers-Kronig analysis are described in the Supplementary Material [23]. Magnetic torque measurements have also been performed on the optimally-doped material.

III. RESULTS AND DISCUSSION

The temperature dependence of the real part of the in-plane optical conductivity [$\sigma_1(\omega)$] is shown in the infrared region for the undoped and doped compounds in Figs. 2(a) and 2(b), respectively; the conductivity is shown over a much broader frequency range in the in-

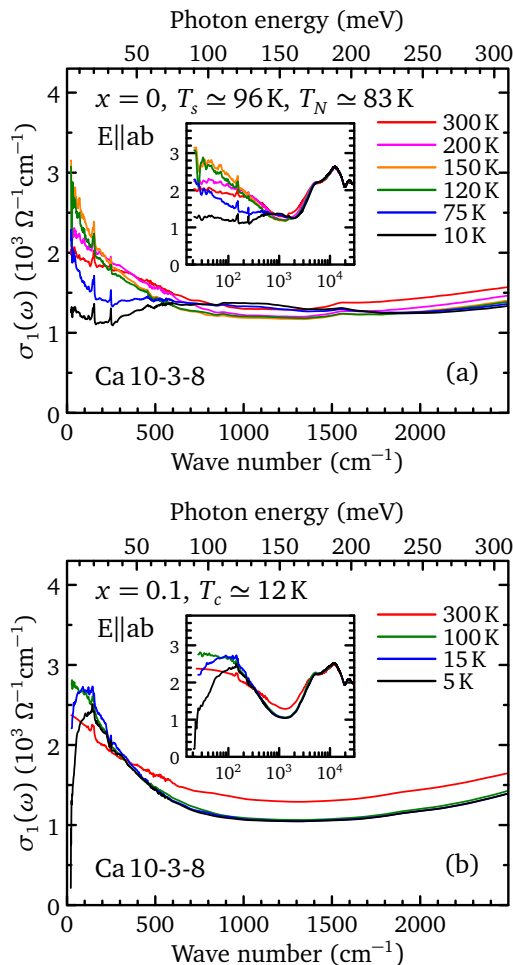


Figure 2. The temperature dependence of the real part of the optical conductivity in the a - b planes of $(\text{CaFe}_{1-x}\text{Pt}_x\text{As})_{10}\text{-Pt}_3\text{As}_8$ for (a) $x = 0$, and (b) $x = 0.1$; the insets show the optical conductivity at several temperatures over a wide frequency range.

sets. Several sharp features in the conductivity are observed at ≈ 150 and 250 cm⁻¹, which are attributed to infrared-active lattice vibrations. The extrapolated values for the dc resistivity [$\sigma_1(\omega \rightarrow 0) \equiv \sigma_{dc}$, circles in Figs. 1(b) and 1(c)] are essentially identical to the resistivity, indicating the excellent agreement between optics and transport measurements.

The FeSCs are multiband materials; a minimal description consists of two electronic subsystems using the so-called two-Drude model [24] with the complex dielectric function $\tilde{\epsilon} = \epsilon_1 + i\epsilon_2$,

$$\tilde{\epsilon}(\omega) = \epsilon_\infty - \sum_{j=1}^2 \frac{\omega_{p,D;j}^2}{\omega^2 + i\omega/\tau_{D,j}} + \sum_k \frac{\Omega_k^2}{\omega_k^2 - \omega^2 - i\omega\gamma_k}, \quad (1)$$

where ϵ_∞ is the real part at high frequency. In the first sum $\omega_{p,D;j}^2 = 4\pi n_j e^2 / m_j^*$ and $1/\tau_{D,j}$ are the square of the plasma frequency and scattering rate for the delocalized (Drude) carriers in the j th band, respectively,

and n_j and m_j^* are the carrier concentration and effective mass. In the second summation, ω_k , γ_k and Ω_k are the position, width, and strength of the k th vibration or bound excitation. The complex conductivity is $\tilde{\sigma}(\omega) = \sigma_1 + i\sigma_2 = -2\pi i\omega[\tilde{\epsilon}(\omega) - \epsilon_\infty]/Z_0$ (in units of $\Omega^{-1}\text{cm}^{-1}$); $Z_0 \approx 377 \Omega$ is the impedance of free space. The model is fit to the real and imaginary parts of the optical conductivity simultaneously using a non-linear least-squares technique.

A. Parent compound ($x = 0$)

At room temperature the optical conductivity in Fig. 2(a) has a metallic character, with a Drude-like free carrier response superimposed on a flat, nearly incoherent background. The results of the two-Drude model fit at 150 K is shown in Fig. 3(a); the conductivity may be described by a free-carrier response consisting of a narrow Drude term that reflects the coherent response, and a much stronger, broad Drude component that corresponds to a nearly incoherent background; several Lorentzian oscillators are included to describe the bound excitations (interband transitions) at higher energies [Fig. 2(a)]. As the temperature is lowered, the low-frequency conductivity is suppressed and a broad peak develops in the mid-infrared region. The results of the model fit at 10 K are shown in Fig. 3(b); while the broad Drude has been reduced slightly in strength, the narrow Drude is strongly suppressed and a strong peak centered at ≈ 1000 cm⁻¹ has emerged.

The temperature dependencies of the scattering rates and the plasma frequencies of the narrow and broad Drude terms are shown in Figs. 3(c) and 3(d), respectively. As the temperature is reduced, the scattering rate for the broad Drude term shows a weak temperature dependence; however, for $T \lesssim T_s, T_N$, it undergoes a dramatic reduction from about ≈ 1600 to ≈ 1000 cm⁻¹. In contrast, the scattering rate for the narrow Drude term has a strong temperature dependence, decreasing from ≈ 660 cm⁻¹ at room temperature to ≈ 180 cm⁻¹ at 100 K, below which it decreases rapidly to ≈ 80 cm⁻¹ at low temperature. The temperature dependence of the plasma frequencies tells a similar story. As the temperature is reduced, the plasma frequency of the broad Drude term is essentially constant; however, for $T \lesssim T_s, T_N$ it undergoes a dramatic reduction, losing roughly 50% of its strength ($\propto \omega_{p,D;i}^2$). At the same time, a broad peak of roughly equal strength appears in the mid-infrared region; as the temperature is further reduced, the strength of both features remains unchanged. The narrow Drude initially shows little temperature dependence, but below about 200 K it begins to decrease uniformly with temperature, showing only a slight discontinuity at the structural and magnetic transitions, ultimately losing over 90% of its original strength at low temperature. Even though the coherent component is losing strength with decreasing temperature, the commensurate decrease in

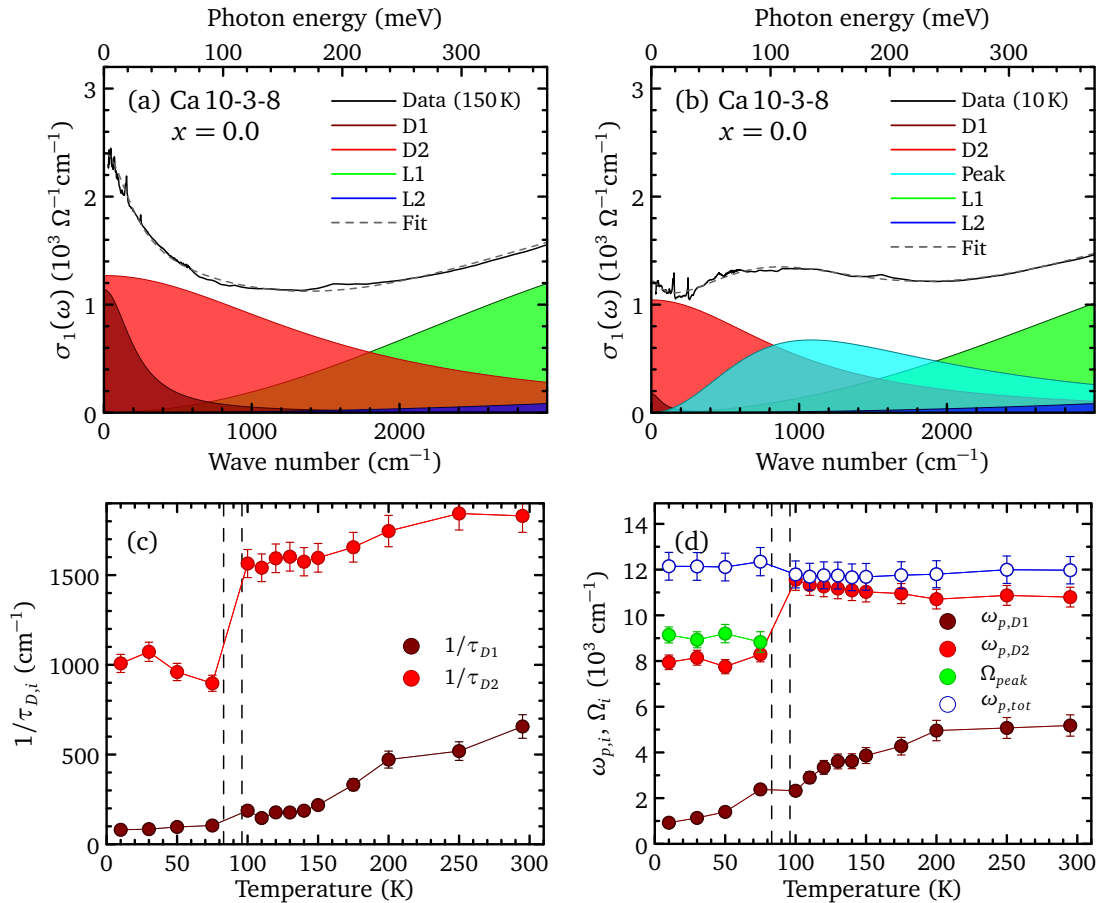


Figure 3. The Drude-Lorentz model fits to $\sigma_1(\omega)$ of the Ca 10-3-8 undoped parent compound at (a) 150 K and (b) 10 K, decomposed into the narrow (D1) and broad (D2) Drude components, as well as several bound excitations; the peak that emerges below $T_s \simeq 96$ K, $T_N \simeq 83$ K (dashed lines) has been fit using a Lorentzian line shape. (c) The temperature dependence of the scattering rates for the narrow and broad Drude components. (d) The plasma frequency for the narrow and broad Drude components, the oscillator strength of the mid-infrared peak, and the total of all three contributions.

the scattering rate results in a slight decrease in the resistivity [Fig. 1(b)], until $\simeq 150$ K, below which the resistivity begins to increase.

These trends may also be observed in the behavior of the spectral weight. The spectral weight is defined here as

$$W(T) = \frac{Z_0}{\pi^2} \int_{\omega_a}^{\omega_b} \sigma_1(\omega, T) d\omega, \quad (2)$$

over the $\omega_a - \omega_b$ interval. As the temperature is lowered, spectral weight is transferred from high to low frequency as the scattering rates decrease, shown in Fig. 4(a). This trend is gradually reversed below $\simeq 150$ K with spectral weight now transferred from below 600 cm^{-1} to a broad peak centered at $\sim 1000 \text{ cm}^{-1}$.

The f -sum rule requires that the sum of the squares of the plasma frequencies, $\omega_{p,tot}^2 = \omega_{p,D1}^2 + \omega_{p,D2}^2 + \Omega_{peak}^2$, should remain constant. This is indeed the case, as shown in Fig. 3(d), so it may be inferred that below T_s and T_N , strength is transferred from both the coherent and incoherent bands into the mid-infrared excitation. This

type of behavior is widely observed in most parent compounds of the FeSCs [25, 26] and is attributed to the formation of a spin-density-wave-like (SDW) gap [27] and subsequent reconstruction of the Fermi surface [28] resulting in low-energy interband transitions that lie in the infrared region. Interestingly, the coherent component begins to lose strength well above the structural and magnetic transitions [Figs.3(d) and 4(a)]. The parent material is highly 2D [29], the interlayer magnetic coupling is very weak, and is easily destroyed by doping [20]. Before three dimensional (3D) long-range AFM order can be established, intralayer 2D short-range AFM fluctuations are present [30, 31]. As a result, the semiconducting-like behavior above T_N may be regarded as the precursor to AFM order.

B. Optimally-doped compound ($x = 0.1$)

In the optimally-doped sample, shown in Fig. 2(b), the optical conductivity exhibits metallic behavior above

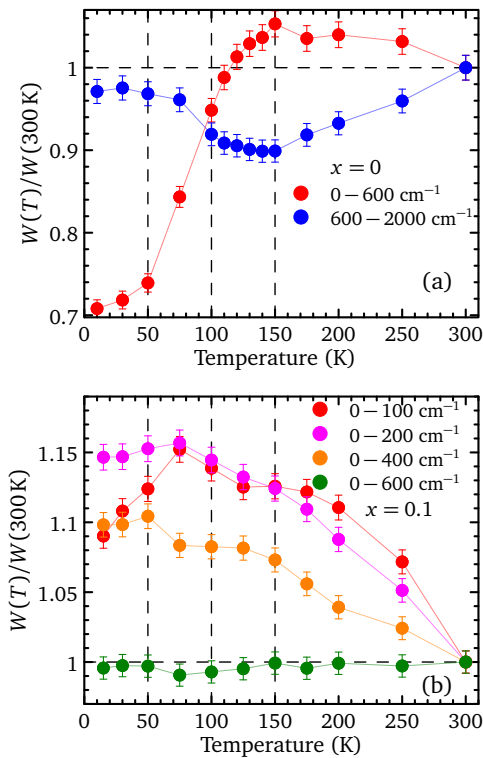


Figure 4. The temperature dependence of the normalized spectral weight in the Ca 10-3-8 for the (a) undoped parent compound and (b) optimally-doped material over several different frequency intervals.

~ 100 K, although its temperature dependence is rather weak, with spectral weight being gradually transferred from high to low frequency. Below 100 K, the spectral weight below 100 cm^{-1} is gradually suppressed while the spectral weight below 600 cm^{-1} remains constant, suggesting that the missing weight is being transferred to the $100 - 600 \text{ cm}^{-1}$ region [Fig. 4(b)], with the formation of a new absorption peak at $\simeq 120 \text{ cm}^{-1}$. At the same time, the low-frequency conductivity is also decreasing, corresponding to the semiconducting-like response below 100 K [Figs. 1(c) and 2(b)]. Upon entry into the superconducting state, the optical conductivity in the low-energy region is almost completely suppressed, with $\sigma_1(\omega) \simeq 0$ below $\sim 20 \text{ cm}^{-1}$, signalling the opening of a nodeless superconducting energy gap [32].

1. Normal state

The results of the fits using the two-Drude model to the conductivity of the optimally-doped sample at 150 and 15 K are summarized in Figs. 5(a) and 5(b), respectively. As observed in the parent compound, at room temperature the conductivity may be described by narrow and broad Drude terms; several Lorentzian oscillators are included to describe the bound excitations (interband transitions) at higher energies [Fig. 2(b)]. Below 100 K, the

decrease in intensity of the narrow Drude component is accompanied by the formation of a peak at $\simeq 120 \text{ cm}^{-1}$ [Fig. 5(b)], which has been fit using a Lorentzian line shape. The temperature dependencies of the scattering rates and plasma frequencies are shown in Figs. 5(c) and 5(d), respectively. By tracking the strengths of the plasma frequencies of the Drude terms, we note that below $T^* \simeq 100$ K the plasma frequency of the narrow Drude is suppressed while the strength of the new peak is gradually enhanced [Fig. 5(d)]; the broad Drude term displays little temperature dependence above or below T^* . The conservation of spectral weight again requires that $\omega_{p,tot}^2 = \omega_{p,D1}^2 + \omega_{p,D2}^2 + \Omega_{peak}^2$ should remain constant, which is indeed the case in Fig. 5(d). Thus, below T^* , some of the coherent response (narrow Drude) is transferred to the new peak in the optical conductivity, resulting in a reduced σ_{dc} and semiconducting-like behavior.

The evolution of the low-energy peak may also be described using a simple classical generalization of the Drude (CGD) formula in which the fraction of the carriers velocity that is retained after a collision [33]. While many collisions may be considered, in the single-scattering approximation the complex conductivity is written as

$$\tilde{\sigma}(\omega) = \left(\frac{2\pi}{Z_0} \right) \frac{\omega_p^2 \tau}{(1 - i\omega\tau)} \left[1 + \frac{c}{(1 - i\omega\tau)} \right], \quad (3)$$

where c is the persistence of velocity that is retained for a single collision. This model has the interesting attribute that for $c = 0$ a simple Drude is recovered, while for $c = -1$ the carriers are completely localized in the form of a Lorentzian oscillator with a peak at $\omega\tau = 1$, width $2/\tau$, and an oscillator strength that is identical to the plasma frequency (Supplemental Material). The real and imaginary parts of the optical conductivity have been fit between 15 and 125 K using the two-Drude model with the provision that the narrow Drude component is replaced by the expression in Eq. (3). At 125 K, the fit is identical to that of the two-Drude model, returning $c = 0$ (pure Drude). Fits below 100 K reveal an increasingly negative value for $c = -0.26, -0.49, -0.41, -0.51$, and -0.61 ± 0.05 at 100, 75, 50, 30, and 15 K, respectively. Interestingly, the plasma frequency for the narrow Drude is now roughly constant, with $\omega_{p,D1} \simeq 5200 \pm 500 \text{ cm}^{-1}$, which is essentially identical to the values returned from the two-Drude model at and above 125 K [Fig. 5(d)]; this indicates that the response of both the localized and free carriers is now incorporated into a single plasma frequency. The scattering rate is also slightly lower at low temperatures than the values obtained using the two-Drude model [Fig. 5(c)]. The values for the broad Drude term are unchanged. While the overall quality of the fits is indistinguishable from the two-Drude model, it is remarkable that the introduction of a single new parameter to the narrow Drude band allows both the position and strength of the low-energy peak to be described quite well, indicating that this peak likely arises from carrier localization due to scattering. In addition, the value

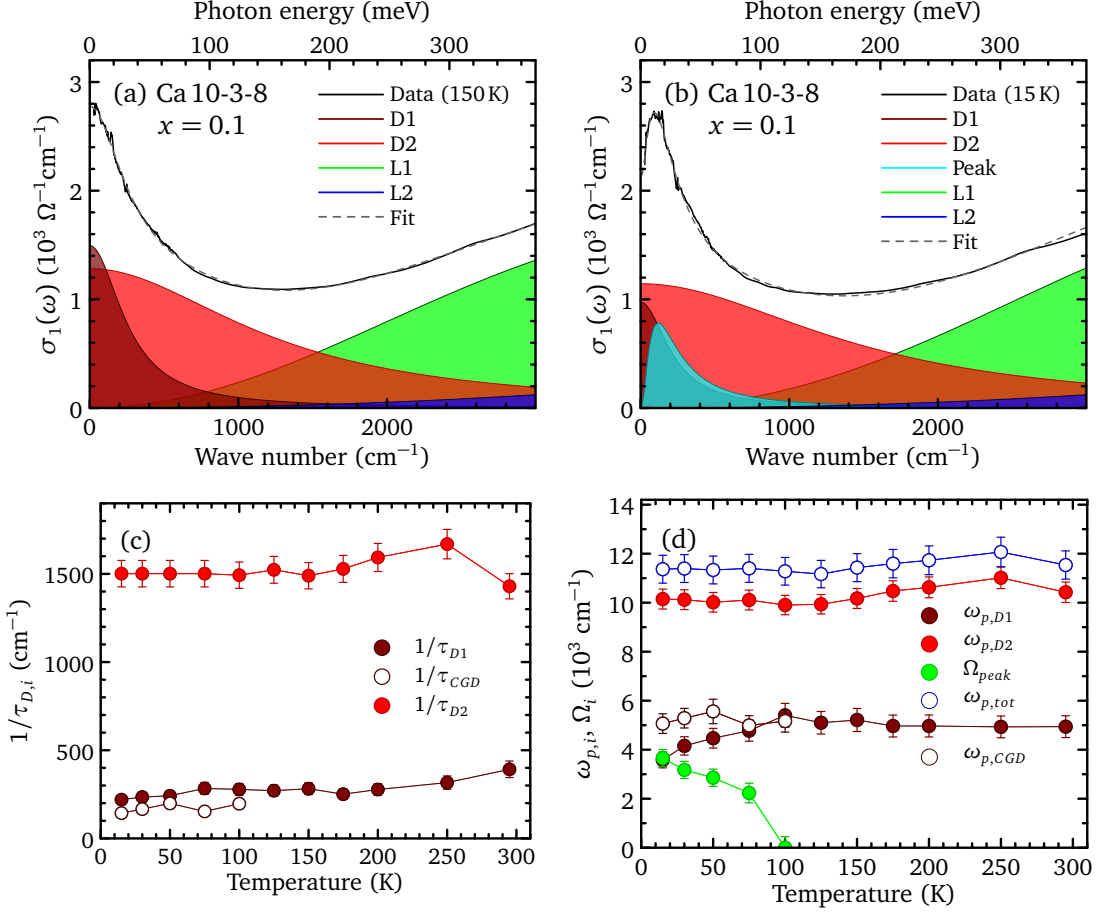


Figure 5. The Drude-Lorentz model fits to $\sigma_1(\omega)$ of the optimally-doped Ca 10-3-8 at (a) 150 K and (b) 15 K, decomposed into the narrow (D1) and broad (D2) Drude components, as well as several bound excitations; the peak that emerges at low temperature has been fit using a Lorentzian line shape. (c) The temperature dependence of the scattering rates for the narrow and broad Drude components for the two-Drude model, as well as that of the classical generalized Drude model (CGD) below $T^* \simeq 100$ K. (d) The plasma frequency for the narrow and broad Drude components, the oscillator strength of the emergent peak, and the total of all three contributions; in the CGD model $\omega_{p,CGD}(T \leq T^*) \simeq \omega_{p,D1}(T > T^*)$.

of $c \simeq -0.6$ at 15 K is consistent with the results of the two-Drude with a Lorentzian that indicate that the spectral weight of the narrow Drude component is split more or less equally between free and localized carriers at low temperature. These results are in good agreement with recent angle-resolved photoemission spectroscopy (ARPES) measurements, which show a clear decrease in the size of the hole pockets below T^* (Supplementary Fig. S2).

2. Superconducting state

Although there is semiconducting-like response in the normal state, below $T_c \simeq 12$ K, the resistivity drops to zero; such a semiconducting-like to superconducting transition is unusual in iron-based superconductors. A clear signature of superconducting transition is observed in the reflectivity [Supplementary Fig. S1(b)]. In the

real part of the optical conductivity, the spectral weight below $\simeq 20 \text{cm}^{-1}$ is totally suppressed, indicating the opening of a nodeless superconducting energy gap. The Mattis-Bardeen formalism is used to describe the gapping of the spectrum of excitations in the superconducting state [34, 35]. The real part of the optical conductivity is shown just above T_c by the dotted line in Fig. 6(a); this curve is described by narrow ($\omega_{p,D1} \simeq 3580 \text{cm}^{-1}$, $1/\tau_{D1} \simeq 220 \text{cm}^{-1}$) and broad ($\omega_{p,D2} \simeq 10150 \text{cm}^{-1}$, $1/\tau_{D2} \simeq 1500 \text{cm}^{-1}$) Drude components, as well as a low-energy bound excitation ($\omega_0 \simeq 120 \text{cm}^{-1}$, $\gamma_0 \simeq 285 \text{cm}^{-1}$, and $\Omega_0 \simeq 3660 \text{cm}^{-1}$). The data below T_c at $\simeq 5$ K is shown by the solid line; despite the presence of multiple bands and a weak shoulder at $\simeq 30 \text{cm}^{-1}$, we have chosen to simplify the analysis and model the data with a single superconducting energy scale for both bands, $2\Delta_1 = 2\Delta_2 \simeq 20 \pm 4 \text{cm}^{-1}$ ($\simeq 2.5 \pm 0.4 \text{meV}$). Note that $1/\tau_{D1} > 2\Delta_{1,2}$, and $1/\tau_{D2} \gg 2\Delta_{1,2}$, placing this material in the dirty limit [36]. The gapped spec-

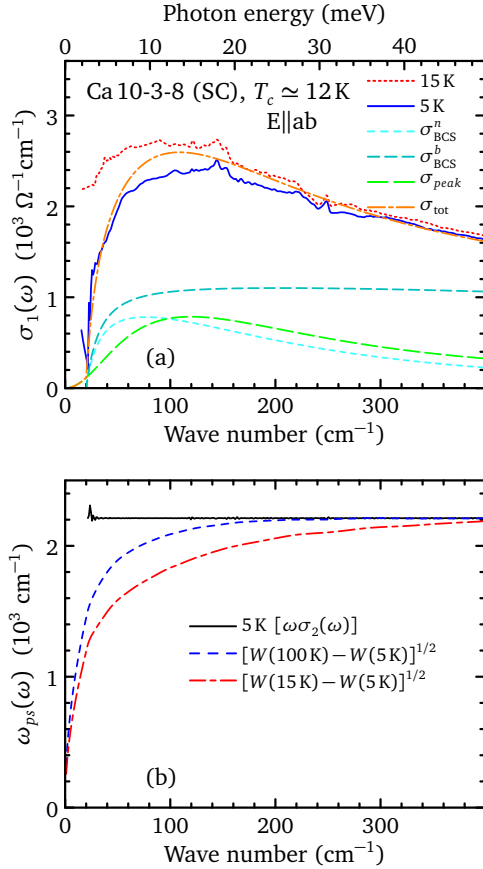


Figure 6. (a) The real part of the optical conductivity of optimally-doped Ca 10-3-8 just above (dotted line) and below (solid line) T_c . The short dashed lines are the gapped spectrum of excitations for the narrow and broad Drude bands with $2\Delta_{1,2} \simeq 20 \text{ cm}^{-1}$; the long dashed line is the contribution of the emergent peak. The linear combination of these contributions (dashed-dot line) reproduces the data quite well, except in the region of peak. (b) The superfluid weight (solid black line) obtained from the imaginary part of $\omega\sigma_2(\omega)$ (see Ref. 37 for details). The red and blue dashed lines are obtained from the FGT sum rule [Eq. (5)].

trum of excitations for the two Drude bands, as well as the contribution from the emergent peak, are shown by the dashed lines in Fig. 6(a). The linear combination of all three contributions reproduces the data quite well, except in the region of the peak. It should be noted that the normal-state values are not refined to fit the data below T_c . The 5 K data may be more accurately reproduced by decreasing the intensity of the peak by about 20%, suggesting that some of the spectral weight of this feature has collapsed into the condensate. The gap ratio $2\Delta_{1,2}/k_B T_c \simeq 2.4$ falls below the BCS value of 3.5, placing this material in the BCS weak-coupling limit

The formation of superconducting energy gap(s) below T_c results in the loss of low-frequency spectral weight that collapses into the superfluid condensate; the strength of the condensate may be estimated in one of two ways. The complex conductivity for the superfluid response may be

expressed as [38, 39]

$$\tilde{\sigma}_s(\omega) = \sigma_{s1} + i\sigma_{s2}(\omega) = \frac{\pi^2}{Z_0} \omega_{ps}^2 \delta(\omega) + \frac{i2\pi\omega_{ps}^2}{Z_0\omega}, \quad (4)$$

where $\omega_{ps}^2 = 4\pi n_s e^2/m^*$ represents the superconducting plasma frequency, n_s is the superconducting carrier density, and m^* is an effective mass. Thus, from the imaginary part $2\pi\omega_{ps}^2 \simeq Z_0\omega\sigma_{s2}(\omega)$. Alternatively, the difference between the low-frequency optical conductivity just above and below T_c , the so-called “missing area”, can be analyzed using the Ferrel-Glover-Tinkham (FGT) sum rule [40, 41]:

$$\frac{Z_0}{\pi^2} \int_{0^+}^{\omega} [\sigma_1(\omega', T \gtrsim T_c) - \sigma_1(\omega', T \ll T_c)] d\omega' = \omega_{ps}^2, \quad (5)$$

where the cutoff frequency ω is chosen so that the integral converges smoothly. Both methods yield similar values of $\omega_{ps} \simeq 2110 \pm 200 \text{ cm}^{-1}$, shown in Fig. 6(b), resulting in a penetration depth of $\lambda_0 = 7500 \pm 600 \text{ \AA}$, in agreement with previous μSR measurements [42].

While about half of the spectral weight of the narrow Drude component has been transferred to the far-infrared absorption peak [Fig. 5(d)], as Fig. 6(a) indicates, this peak is also suppressed below T_c . A key question is: What becomes of these localized electrons? To address this question, we have applied the FGT sum rule by taking the difference in the optical conductivity between 15 and 5 K, and 100 and 5 K. From the results shown in Fig. 6(b), we notice that the superfluid stiffness calculated with respect to 15 and 5 K converge at $\omega \simeq 400 \text{ cm}^{-1}$ ($\sim 50 \text{ meV}$). However, between 100 and 5 K the integral converges much more quickly ($\omega \lesssim 200 \text{ cm}^{-1}$), a very unusual situation. If only the Drude components condense into the superfluid, the results calculated between 15 and 5 K would converge more quickly, because the Drude component is narrower at low temperature [Figs. 5(c) and 5(d)]. Such anomalous behavior suggests that there is an extra component in the 100 – 400 cm^{-1} region that contributes to the superfluid below T_c . This implies that the newly-formed peak below 100 K contributes to the superfluid condensate. Understanding the origin of this peak may provide insight into the unconventional pairing in this material.

In order to further understand the relation between the semiconducting-like behavior and superconductivity, we performed a magnetic torque measurement on the optimally-doped sample (details are provided in the Supplementary Material). In Fig. 7(a), we observe that, below T^* , the torque τ_0 starts to deviate from the high-temperature T -linear behavior and $|\chi_c - \chi_{ab}|$ increases with decreasing H [Fig. 7(b)]. Both types of behavior indicate a non-linear susceptibility [43]. Approaching T_c , this non-linearity appears to diverge in the zero-field limit, suggesting that this behavior may be related to superconducting fluctuations [44]. Inelastic neutron scattering and nuclear magnetic resonance have both observed evidence for preformed Cooper pairs in Ca 10-3-8 [42], and the minimum in the temperature-dependent

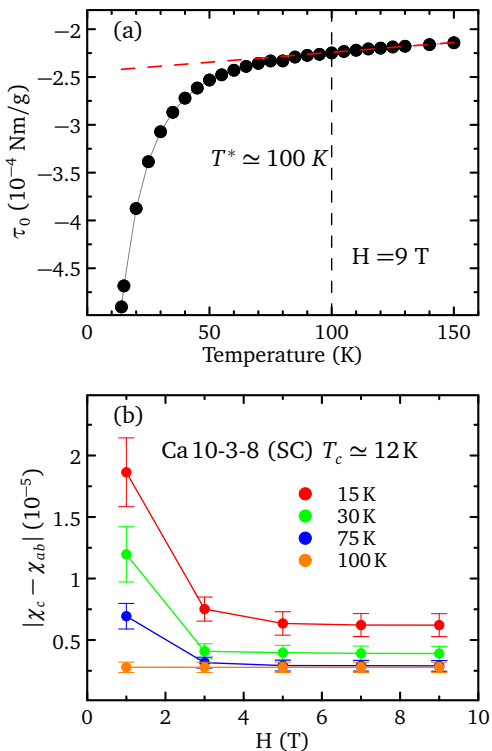


Figure 7. (a) The temperature-dependent out-of-plane torque $\tau_0 = \frac{1}{2}\mu_0(\chi_c - \chi_{ab})H^2$ for the optimally-doped Ca 10-3-8 with fixed magnetic field (9 T); χ_c and χ_{ab} are magnetic susceptibilities along the c and a axis, respectively. The dashed line is linear fit to the high-temperature data. (b) The field-dependent $|\chi_c - \chi_{ab}|$ at different temperatures.

Seebeck coefficient of Pt-doped material can be understood in terms of either preformed pairs or the phonon drag effect [14]. A difficulty with the notion of preformed pairs is that they are typically observed in strong-coupling systems, in which the coherence length is comparable with the inter-particle distance [44]; however, optimally-doped Ca 10-3-8 is in the BCS weak-coupling limit. Furthermore, in cuprates and FeSe, superconducting fluctuations always result in a decrease in the resistance [45]; the semiconducting-like behavior is anomalous.

C. Localization and magnetism

The substitution of Pt for Fe into the Fe-As planes of $(\text{CaFe}_{1-x}\text{Pt}_x\text{As})_{10}\text{Pt}_3\text{As}_8$ induces superconductivity; however, it also results in the introduction of disorder sites that can lead to strong scattering and the localization of free-carriers. In systems that display activated behavior, the interplay between localization and superconductivity is of considerable interest [46, 47]. In $\text{YBa}_2(\text{Cu}_{1-x}\text{Zn}_x)_4\text{O}_8$, the substitution of Zn for Cu led to the dramatic reduction of T_c and the appearance of a peak in the optical conductivity at $\simeq 120 \text{ cm}^{-1}$ that

was attributed to quasiparticle localization [48]. In the cuprates, non-magnetic Zn is thought to act as a magnetic impurity. A low-energy peak in the optical conductivity was also observed when the magnetic impurities Mn and Cr were substituted for Fe in BaFe_2As_2 [49]. However, in $(\text{CaFe}_{1-x}\text{Pt}_x\text{As})_{10}\text{Pt}_3\text{As}_8$, the Pt^{4+} atoms in the Fe-As layers are nonmagnetic and a low-energy peak has never been observed in iron-based superconductors with nonmagnetic impurities [50]. We note that the semiconducting-like behavior is not distinct to Pt-doped Ca 10-3-8; under pressure, the stoichiometric parent compound also shows semiconducting-like behavior, right up to the point at which it becomes a superconductor. The similarity between the phase diagrams of Pt-doped Ca10-3-8, and Ca 10-3-8 under pressure, indicates the intrinsic nature of the semiconducting-like behavior. Moreover, the low-energy peak observed in Pt-doped Ca 10-3-8, has also been seen in La-doped $\text{Ca}_{8.5}\text{La}_{1.5}(\text{Pt}_3\text{As}_8)(\text{Fe}_2\text{As}_2)_5$ (out-of-plan doping) [51], and in stoichiometric $(\text{CaFeAs})_{10}\text{Pt}_4\text{As}_8$ [52]. The 2D nature of these materials will greatly increase the importance of spin fluctuations, suggesting that they may be playing a prominent role in the in-plane transport properties. It is therefore likely that the localization peak observed in this work arises from strong scattering due to AFM fluctuations rather than impurity scattering.

Although AFM order competes with superconductivity, spin fluctuations have been proposed as a possible pairing mechanism in the high-temperature superconductors [53]. The torque magnetometry results [Fig. 7(a)] indicate that the onset for superconducting fluctuations occur well above T_c . This type of behavior has been observed in many high-temperature superconductors [54, 55], and it has been suggested that these fluctuations may be attributed to the inhomogeneous nature (either structural or electronic) of these materials [56]. Thus, it may be the case that the putative normal-state is an effective medium in which the superconducting regions are embedded in a poorly-conducting matrix with either strong spin fluctuations or magnetic order (i.e., incommensurate SDW); below T_c , phase coherence is established across the different superconducting regions and a bulk superconducting transition is observed. The global onset of superconductivity would naturally suppress the magnetic fluctuations (order) and the scattering attributed to it, leading to a reduction in the size of the localization peak. The carriers that are no longer localized due to strong scattering would then be allowed to collapse into the condensate, a result that is consistent with the observed transfer of spectral weight from the peak into the condensate below T_c .

IV. SUMMARY

To conclude, the temperature dependence of the in-plane optical properties of $(\text{CaFe}_{1-x}\text{Pt}_x\text{As})_{10}\text{Pt}_3\text{As}_8$ has been examined for the undoped ($x = 0$) parent compound

with $T_s \simeq 96$ K and $T_N \simeq 83$ K, and the optimally-doped ($x = 0.1$) superconducting material, $T_c \simeq 12$ K. At room temperature, the optical conductivity of both materials may be described by the two-Drude model. In the parent compound, below T_s and T_N the broad Drude component narrows and decreases dramatically in strength, behavior which is also observed in the narrow Drude component. The missing spectral weight is transferred to a broad peak at $\simeq 1000$ cm^{-1} , which is attributed to a low-energy interband transition that originates from the Fermi surface reconstruction driven by the structural and magnetic transitions. The semiconducting-like behavior originates from short-range magnetic fluctuations that could be regarded as the precursor to AFM order. In the optimally-doped material, the broad Drude term shows little temperature dependence, but the scattering rate in the narrow Drude component has a weak temperature dependence. Below $T^* \simeq 100$ K, the narrow Drude loses strength at the same time a localization peak at $\simeq 120$ cm^{-1} emerges. A classical generalization of the Drude model reproduces the position and strength of the low-energy peak, indicating that it originates via a localization process. Torque magnetometry detects a dia-

magnetic signal well above T_c , which is attributed to SC fluctuations. Below T_c magnetic fluctuations (order) are suppressed, resulting in a decrease in localization, allowing spectral weight from this peak to be transferred into the superconducting condensate. These results indicate an intimate relationship between magnetism and superconductivity in this material.

ACKNOWLEDGMENTS

We thank Liling Sun, Jimin Zhao, Weiguo Yin, Yilin Wang, Hu Miao, Peter Johnson for useful discussions. Work at Chinese Academy of Science was supported by NSFC (Project No. 11374345 and No. 91421304) and MOST (Project No. 2015CB921303 and No. 2015CB921102). J.H. acknowledges the financial support from the National Research Foundation of Korea (NRFK Grant No. 2017R1A2B4007387). Work at Brookhaven National Laboratory was supported by the Office of Science, U.S. Department of Energy under Contract No. DE-SC0012704.

-
- [1] David C. Johnston, “The puzzle of high temperature superconductivity in layered iron pnictides and chalcogenides,” *Adv. Phys.* **59**, 803–1061 (2010).
- [2] Johnpierre Paglione and Richard L. Greene, “High-temperature superconductivity in iron-based materials,” *Nat. Phys.* **6**, 645–658 (2010).
- [3] Qimiao Si, Rong Yu, and Elihu Abrahams, “High-temperature superconductivity in iron pnictides and chalcogenides,” *Nat. Rev. Mater.* **1**, 16017 (2016).
- [4] Patrick A. Lee, Naoto Nagaosa, and Xiao-Gang Wen, “Doping a Mott insulator: Physics of high-temperature superconductivity,” *Rev. Mod. Phys.* **78**, 17–85 (2006).
- [5] Qisi Wang, Yao Shen, Bingying Pan, Yiqing Hao, Mingwei Ma, Fang Zhou, P. Steffens, K. Schmalzl, T. R. Forrest, M. Abdel-Hafez, Xiaojia Chen, D. A. Chareev, A. N. Vasiliev, P. Bourges, Y. Sidis, Huibo Cao, and Jun Zhao, “Strong interplay between stripe spin fluctuations, nematicity and superconductivity in FeSe,” *Nat. Mater.* **15**, 159–163 (2016).
- [6] N. E. Hussey, K. Takenaka, and H. Takagi, “Universality of the Mott-Ioffe-Regel limit in metals,” *Phil. Mag.* **84**, 2847–2864 (2004).
- [7] C. M. Varma, P. B. Littlewood, S. Schmitt-Rink, E. Abrahams, and A. E. Ruckenstein, “Phenomenology of the normal state of Cu-O high-temperature superconductors,” *Phys. Rev. Lett.* **63**, 1996–1999 (1989).
- [8] Tom Timusk and Bryan Statt, “The pseudogap in high-temperature superconductors: an experimental survey,” *Rep. Prog. Phys.* **62**, 61 (1999).
- [9] H.-B. Yang, J. D. Rameau, P. D. Johnson, T. Valla, A. Tsvetlik, and G. D. Gu, “Emergence Of Preformed Cooper Pairs From The Doped Mott Insulating State In $\text{Bi}_2\text{Sr}_2\text{CaCu}_2\text{O}_{8+\delta}$,” *Nature (London)* **456**, 77–80 (2008).
- [10] Yayu Wang, Lu Li, M. J. Naughton, G. D. Gu, S. Uchida, and N. P. Ong, “Field-enhanced diamagnetism in the pseudogap state of the cuprate $\text{Bi}_2\text{Sr}_2\text{CaCu}_2\text{O}_{8+\delta}$ superconductor in an intense magnetic field,” *Phys. Rev. Lett.* **95**, 247002 (2005).
- [11] Z. A. Xu, N. P. Ong, Y. Wang, T. Kakeshita, and S. Uchida, “Vortex-like excitations and the onset of superconducting phase fluctuation in underdoped $\text{La}_{2-x}\text{Sr}_x\text{CuO}_4$,” *Nature (London)* **406**, 486–488 (2000).
- [12] T. Valla, A. V. Fedorov, J. Lee, J. C. Davis, and G. D. Gu, “The Ground State of the Pseudogap in Cuprate Superconductors,” *Science* **314**, 1914–1916 (2006).
- [13] R. M. Fernandes, A. V. Chubukov, J. Knolle, I. Eremin, and J. Schmalian, “Preemptive nematic order, pseudogap, and orbital order in the iron pnictides,” *Phys. Rev. B* **85**, 024534 (2012).
- [14] N. Ni, J. M. Allred, B. C. Chan, and R. J. Cava, “High T_c electron doped $\text{Ca}_{10}(\text{Pt}_3\text{As}_8)(\text{Fe}_2\text{As}_2)_5$ and $\text{Ca}_{10}(\text{Pt}_4\text{As}_8)(\text{Fe}_2\text{As}_2)_5$ superconductors with skutterudite intermediary layers,” *PNAS* **108**, E1019–E1026 (2011).
- [15] Peiwen Gao, Liling Sun, Ni Ni, Jing Guo, Qi Wu, Chao Zhang, Dachun Gu, Ke Yang, Aiguo Li, Sheng Jiang, Robert Joseph Cava, and Zhongxian Zhao, “Pressure-Induced Superconductivity and Its Scaling with Doping-Induced Superconductivity in the Iron Pnictide with Skutterudite Intermediary Layers,” *Adv. Mat.* **26**, 2346–2351 (2014).
- [16] K. Cho, M. A. Tanatar, H. Kim, W. E. Straszheim, N. Ni, R. J. Cava, and R. Prozorov, “Doping-dependent superconducting gap anisotropy in the two-dimensional pnictide $\text{Ca}_{10}(\text{Pt}_3\text{As}_8)[(\text{Fe}_{1-x}\text{Pt}_x)_2\text{As}_2]_5$,” *Phys. Rev. B* **85**, 020504(R) (2012).

- [17] T. Zhou, G. Koutroulakis, J. Lodico, Ni Ni, J. D. Thompson, R. J. Cava, and S. E. Brown, “Antiferromagnetic order in $\text{Ca}_{10}(\text{Pt}_3\text{As}_8)(\text{Fe}_2\text{As}_2)_5$ observed by ^{75}As NMR,” *J Phys.: Condens. Matter* **25**, 122201 (2013).
- [18] T. Strürzer, G. M. Friederichs, H. Luetkens, A. Amato, H.-H. Klauss, and Dirk Johrendt, “Structural and magnetic phase transitions in triclinic $\text{Ca}_{10}(\text{FeAs})_{10}(\text{Pt}_3\text{As}_8)$,” *J. Phys.: Condens. Matter* **25**, 122203 (2013).
- [19] A. Sapkota, G. S. Tucker, M. Ramazanoglu, W. Tian, N. Ni, R. J. Cava, R. J. McQueeney, A. I. Goldman, and A. Kreyssig, “Lattice distortion and stripelike antiferromagnetic order in $\text{Ca}_{10}(\text{Pt}_3\text{As}_8)(\text{Fe}_2\text{As}_2)_5$,” *Phys. Rev. B* **90**, 100504(R) (2014).
- [20] Z. J. Xiang, X. G. Luo, J. J. Ying, X. F. Wang, Y. J. Yan, A. F. Wang, P. Cheng, G. J. Ye, and X. H. Chen, “Transport properties and electronic phase diagram of single-crystalline $\text{Ca}_{10}(\text{Pt}_3\text{As}_8)((\text{Fe}_{1-x}\text{Pt}_x)_2\text{As}_2)_5$,” *Phys. Rev. B* **85**, 224527 (2012).
- [21] N. Ni, W. E. Straszheim, D. J. Williams, M. A. Tanatar, R. Prozorov, E. D. Bauer, F. Ronning, J. D. Thompson, and R. J. Cava, “Transport and thermodynamic properties of $(\text{Ca}_{1-x}\text{La}_x)_{10}(\text{Pt}_3\text{As}_8)(\text{Fe}_2\text{As}_2)_5$ superconductors,” *Phys. Rev. B* **87**, 060507(R) (2013).
- [22] Christopher C. Homes, M. Reedyk, D. A. Crandles, and T. Timusk, “Technique for measuring the reflectance of irregular, submillimeter-sized samples,” *Appl. Opt.* **32**, 2976–2983 (1993).
- [23] See Supplemental Material at [URL will be inserted by publisher] for details of the experimental reflectivity and Kramers-Kronig analysis; classical generalization of the Drude model; angle resolved photoemission spectroscopy of the optimally-doped material; determination of the superfluid response; and magnetic torque experiments, which includes Refs. ? ? ? .
- [24] D. Wu, N. Barišić, P. Kallina, A. Faridian, B. Gorshunov, N. Drichko, L. J. Li, X. Lin, G. H. Cao, Z. A. Xu, N. L. Wang, and M. Dressel, “Optical investigations of the normal and superconducting states reveal two electronic subsystems in iron pnictides,” *Phys. Rev. B* **81**, 100512(R) (2010).
- [25] Masamichi Nakajima, Shigeyuki Ishida, Takahide Tanaka, Kunihiro Kihou, Yasuhide Tomioka, Taku Saito, Chul-Ho Lee, Hideto Fukazawa, Yoh Kohori, Teruhisa Kakeshita, Akira Iyo, Toshimitsu Ito, Hiroshi Eisaki, and Shin-ichi Uchida, “Strong Electronic Correlations in Iron Pnictides: Comparison of Optical Spectra for BaFe_2As_2 -Related Compounds,” *J. Phys. Soc. Jpn.* **83**, 104703 (2014).
- [26] Y. M. Dai, Ana Akrap, S. L. Bud’ko, P. C. Canfield, and C. C. Homes, “Optical properties of AFe_2As_2 ($A = \text{Ca}, \text{Sr},$ and Ba) single crystals,” *Phys. Rev. B* **94**, 195142 (2016).
- [27] W. Z. Hu, J. Dong, G. Li, Z. Li, P. Zheng, G. F. Chen, J. L. Luo, and N. L. Wang, “Origin of the Spin Density Wave Instability in AFe_2As_2 ($A = \text{Ba}, \text{Sr}$) as Revealed by Optical Spectroscopy,” *Phys. Rev. Lett.* **101**, 257005 (2008).
- [28] Z. P. Yin, K. Haule, and G. Kotliar, “Magnetism and charge dynamics in iron pnictides,” *Nat. Phys.* **7**, 294–297 (2011).
- [29] F. F. Yuan, Y. Sun, W. Zhou, X. Zhou, Q. P. Ding, K. Iida, R. Hühne, L. Schultz, T. Tamegai, and Z. X. Shi, “Anisotropy of iron-platinum-arsenide $\text{Ca}_{10}(\text{Pt}_n\text{As}_8)(\text{Fe}_{2-x}\text{Pt}_x\text{As}_2)_5$ single crystals,” *App. Phys. Lett.* **107**, 012602 (2015).
- [30] Pengcheng Dai, Jiangping Hu, and Elbio Dagotto, “Magnetism and its microscopic origin in iron-based high-temperature superconductors,” *Nat. Phys.* **8**, 709–718 (2012).
- [31] B. Xu, Y. M. Dai, H. Xiao, B. Shen, Z. R. Ye, A. Forget, D. Colson, D. L. Feng, H. H. Wen, X. G. Qiu, and R. P. S. M. Lobo, “Optical observation of spin-density-wave fluctuations in Ba122 iron-based superconductors,” *Phys. Rev. B* **94**, 085147 (2016).
- [32] Run Yang, Yaomin Dai, Bing Xu, Wei Zhang, Ziyang Qiu, Qiangtao Sui, Christopher C. Homes, and Xiang-gang Qiu, “Anomalous phonon behavior in superconducting $\text{CaKFe}_4\text{As}_4$: An optical study,” *Phys. Rev. B* **95**, 064506 (2017).
- [33] N. V. Smith, “Classical generalization of the Drude formula for the optical conductivity,” *Phys. Rev. B* **64**, 155106 (2001).
- [34] W. Zimmermann, E.H. Brandt, M. Bauer, E. Seider, and L. Genzel, “Optical conductivity of BCS superconductors with arbitrary purity,” *Physica C* **183**, 99–104 (1991).
- [35] M. Dressel and G. Grüner, *Electrodynamics of Solids* (Cambridge University Press, Cambridge, 2001).
- [36] C. C. Homes, Y. M. Dai, J. S. Wen, Z. J. Xu, and G. D. Gu, “ $\text{FeTe}_{0.55}\text{Se}_{0.45}$: A multiband superconductor in the clean and dirty limit,” *Phys. Rev. B* **91**, 144503 (2015).
- [37] C. C. Homes, S. V. Dordevic, D. A. Bonn, Ruixing Liang, and W. N. Hardy, “Sum rules and energy scales in the high-temperature superconductor $\text{YBa}_2\text{Cu}_3\text{O}_{6+x}$,” *Phys. Rev. B* **69**, 024514 (2004).
- [38] S. V. Dordevic, E. J. Singley, D. N. Basov, Seiki Komiya, Yoichi Ando, E. Bucher, C. C. Homes, and M. Strongin, “Global trends in the interplane penetration depth of layered superconductors,” *Phys. Rev. B* **65**, 134511 (2002).
- [39] J. Hwang, T. Timusk, and G. D. Gu, “Doping dependent optical properties of $\text{Bi}_2\text{Sr}_2\text{CaCu}_2\text{O}_{8+\delta}$,” *J. Phys.: Condens. Matter* **19**, 125208 (2007).
- [40] Richard A. Ferrell and Rolfe E. Glover, “Conductivity of Superconducting Films: A Sum Rule,” *Phys. Rev.* **109**, 1398–1399 (1958).
- [41] M. Tinkham and R. A. Ferrell, “Determination of the Superconducting Skin Depth from the Energy Gap and Sum Rule,” *Phys. Rev. Lett.* **2**, 331–333 (1959).
- [42] M. A. Surmach, F. Brückner, S. Kamusella, R. Sarkar, P. Y. Portnichenko, J. T. Park, G. Ghambashidze, H. Luetkens, P. K. Biswas, W. J. Choi, Y. I. Seo, Y. S. Kwon, H.-H. Klauss, and D. S. Inosov, “Superconducting properties and pseudogap from preformed cooper pairs in the triclinic $(\text{CaFe}_{1-x}\text{Pt}_x\text{As})_{10}\text{Pt}_3\text{As}_8$,” *Phys. Rev. B* **91**, 104515 (2015).
- [43] H. Xiao, T. Hu, W. Zhang, Y. M. Dai, H. Q. Luo, H. H. Wen, C. C. Almasan, and X. G. Qiu, “Two distinct superconducting fluctuation diamagnetisms in $\text{Bi}_2\text{Sr}_{2-x}\text{La}_x\text{CuO}_{6+\delta}$,” *Phys. Rev. B* **90**, 214511 (2014).
- [44] S. Kasahara, T. Yamashita, A. Shi, R. Kobayashi, Y. Shimoyama, T. Watashige, K. Ishida, T. Terashima, T. Wolf, F. Hardy, C. Meingast, H. v. Löhneysen, A. Levchenko, T. Shibauchi, and Y. Matsuda, “Giant superconducting fluctuations in the compensated semimetal FeSe at the BCS–BEC crossover,” *Nat. Commun.* **7**, 12843 (2016).
- [45] Petar Popčević, Damjan Pelc, Yang Tang, Kristijan Velebit, Zachary Anderson, Vikram Nagarajan, Nagara-

- jan Yu, Miroslav Požek, Neven Barišić, and Martin Greven, “Percolative nature of the direct-current conductivity in cuprate superconductors,” *npj Quantum Materials* **3**, 42 (2018).
- [46] Michael Ma and Patrick A. Lee, “Localized superconductors,” *Phys. Rev. B* **32**, 5658–5667 (1985).
- [47] J. M. Valles, A. E. White, K. T. Short, R. C. Dynes, J. P. Garno, A. F. J. Levi, M. Anzlowar, and K. Baldwin, “Ion-beam-induced metal-insulator transition in $\text{YBa}_2\text{Cu}_3\text{O}_{7-\delta}$: A mobility edge,” *Phys. Rev. B* **39**, 11599–11602 (1989).
- [48] D. N. Basov, B. Dabrowski, and T. Timusk, “Infrared Probe of Transition from Superconductor to Nonmetal in $\text{YBa}_2(\text{Cu}_{1-x}\text{Zn}_x)_4\text{O}_8$,” *Phys. Rev. Lett.* **81**, 2132–2135 (1998).
- [49] T. Kobayashi, M. Nakajima, S. Miyasaka, and S. Tajima, “Carrier localization due to local magnetic order induced by magnetic impurities in $\text{Ba}(\text{Fe}_{1-x}\text{TM}_x)_2\text{As}_2$ (TM = Mn and Cr) as seen via optical spectra,” *Phys. Rev. B* **94**, 224516 (2016).
- [50] M. Nakajima, S. Ishida, K. Kihou, Y. Tomioka, T. Ito, Y. Yoshida, C. H. Lee, H. Kito, A. Iyo, H. Eisaki, K. M. Kojima, and S. Uchida, “Evolution of the optical spectrum with doping in $\text{Ba}(\text{Fe}_{1-x}\text{Co}_x)_2\text{As}_2$,” *Phys. Rev. B* **81**, 104528 (2010).
- [51] Yu-il Seo, Woo-Jae Choi, Shin-ichi Kimura, Yunkyung Bang, and Yong Seung Kwon, “Optical properties of optimally doped single-crystal $\text{Ca}_{8.5}\text{La}_{1.5}(\text{Pt}_3\text{As}_8)(\text{Fe}_2\text{As}_2)_5$,” *Phys. Rev. B* **95**, 094510 (2017).
- [52] Y. I. Seo, W. J. Choi, S. i. Kimura, and Y. S. Kwon, “Evidence for a preformed Cooper pair model in the pseudogap spectra of a $\text{Ca}_{10}(\text{Pt}_4\text{As}_8)(\text{Fe}_2\text{As}_2)_5$ single crystal with a nodal superconducting gap,” *Sci. Rep.* **9**, 3987 (2019).
- [53] Toru Moriya and Kazuo Ueda, “Spin fluctuations and high temperature superconductivity,” *Adv. Phys.* **49**, 555–606 (2000).
- [54] Lu Li, Yayu Wang, Seiki Komiya, Shimpei Ono, Yoichi Ando, G. D. Gu, and N. P. Ong, “Diamagnetism and Cooper pairing above T_c in cuprates,” *Phys. Rev. B* **81**, 054510 (2010).
- [55] O. Cyr-Choinière, R. Daou, F. Laliberté, C. Collignon, S. Badoux, D. LeBoeuf, J. Chang, B. J. Ramshaw, D. A. Bonn, W. N. Hardy, R. Liang, J.-Q. Yan, J.-G. Cheng, J.-S. Zhou, J. B. Goodenough, S. Pyon, T. Takayama, H. Takagi, N. Doiron-Leyraud, and Louis Taillefer, “Pseudogap temperature T^* of cuprate superconductors from the Nernst effect,” *Phys. Rev. B* **97**, 064502 (2018).
- [56] Damjan Pelc, Marija Vučković, Mihael S. Grbić, Miroslav Požek, Guichuan Yu, Takao Sasagawa, Martin Greven, and Neven Barišić, “Emergence of superconductivity in the cuprates via a universal percolation process,” *Nat. Commun.* **9**, 4327 (2018).

Supplementary material for: Unraveling the mechanism of the semiconducting-like behavior and its relation to superconductivity in $(\text{CaFe}_{1-x}\text{Pt}_x\text{As})_{10}\text{Pt}_3\text{As}_8$

Run Yang,^{1,2,3} Yaomin Dai,⁴ Jia Yu,^{1,3} Qiangtao Sui,^{1,3} Yongqing Cai,^{1,3} Zhian Ren,^{1,3,5} Jungseek Hwang,^{2,6} Hong Xiao,⁷ Xingjiang Zhou,^{1,3,5} Xianggang Qiu,^{1,3,5,*} and Christopher C. Homes^{2,†}

¹Beijing National Laboratory for Condensed Matter Physics,
Institute of Physics, Chinese Academy of Sciences, Beijing 100190, China

²Condensed Matter Physics and Materials Science Division,
Brookhaven National Laboratory, Upton, New York 11973, USA

³School of Physical Sciences, University of Chinese Academy of Sciences, Beijing 100049, China

⁴Center for Superconducting Physics and Materials,

National Laboratory of Solid State Microstructures and Department of Physics, Nanjing University, Nanjing 210093, China

⁵Collaborative Innovation Center of Quantum Matter, Beijing 100084, China

⁶Department of Physics, Sungkyunkwan University, Suwon, Gyeonggi-do 16419, Korea

⁷Center for High Pressure Science and Technology Advanced Research, Beijing 100094, China

EXPERIMENTAL DETAILS

High-quality single crystals of $(\text{CaFe}_{1-x}\text{Pt}_x\text{As})_{10}\text{Pt}_3\text{As}_8$ (Ca 10-3-8) with good cleavage planes (001) were synthesized using self-flux method [1] for $x = 0$ and 0.1. The resistivity measurements were performed using a Quantum Design Physical Property Measurement System (PPMS). The reflectivity from a freshly-cleaved surface has been measured at a near-normal angle of incidence using Fourier transform infrared spectrometers (Bruker Vertex 80v and IFS 113v) for light polarized in the a - b plane using an *in situ* evaporation technique [2]. Data from ~ 15 to $45\,000\text{ cm}^{-1}$ were collected at different temperatures from ~ 5 to 300 K using an ARS Helitran open-flow cryostat. The optical conductivity has been determined from a Kramers-Kronig analysis of the reflectivity $R(\omega)$. Because the measurement is performed over a finite energy range, extrapolations are necessary for $\omega \rightarrow 0, \infty$ [3]. Below the lowest measured frequency, the Hagen-Rubens relation [$R(\omega) = 1 - A\sqrt{\omega}$] for a metal is used, while above the highest-measured frequency ($42\,000\text{ cm}^{-1}$), $R(\omega)$ is assumed to be constant up to 10 eV , above which a free-electron response ($\propto \omega^{-4}$) is used [4].

Figures S1(a) and S1(b) show the temperature dependence of the reflectivity $R(T, \omega)$ of the undoped and optimally-doped samples. In the far-infrared region, at high temperature, both display a typical metallic response, with the reflectivity approaching unity at zero frequency and increasing upon cooling. However, for the parent compound, below $T^* \simeq 150\text{ K}$, the reflectance below 1000 cm^{-1} is suppressed continuously with decreasing temperature. For the optimally-doped sample, below $T^* \simeq 100\text{ K}$, similar behavior is also observed for the reflectivity below 100 cm^{-1} , but

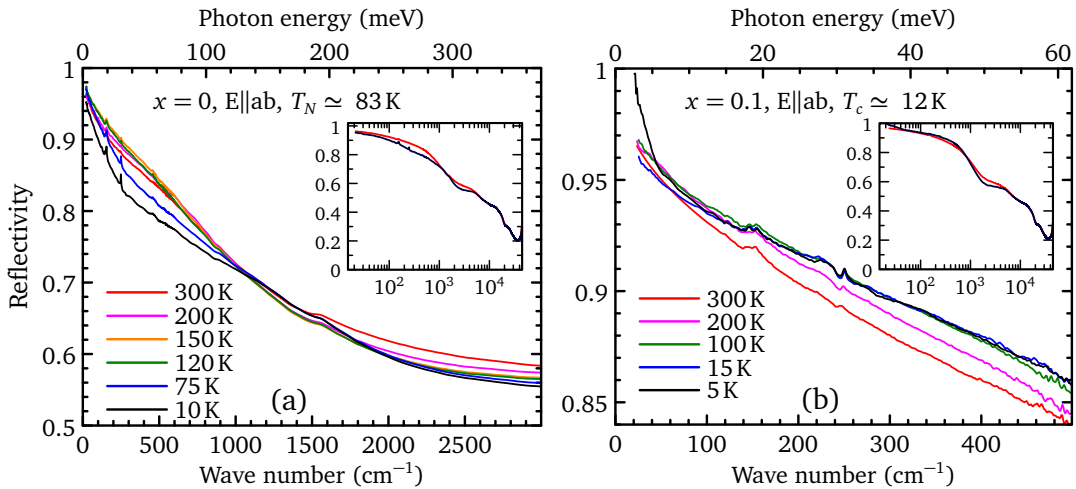


Figure S1. Temperature-dependent reflectivity of the (a) undoped, and (b) optimally doped Ca 10-3-8 materials in the far-infrared region for light polarized in the Fe-As planes. Insets: the reflectivity in the high-frequency range at high and low temperatures.

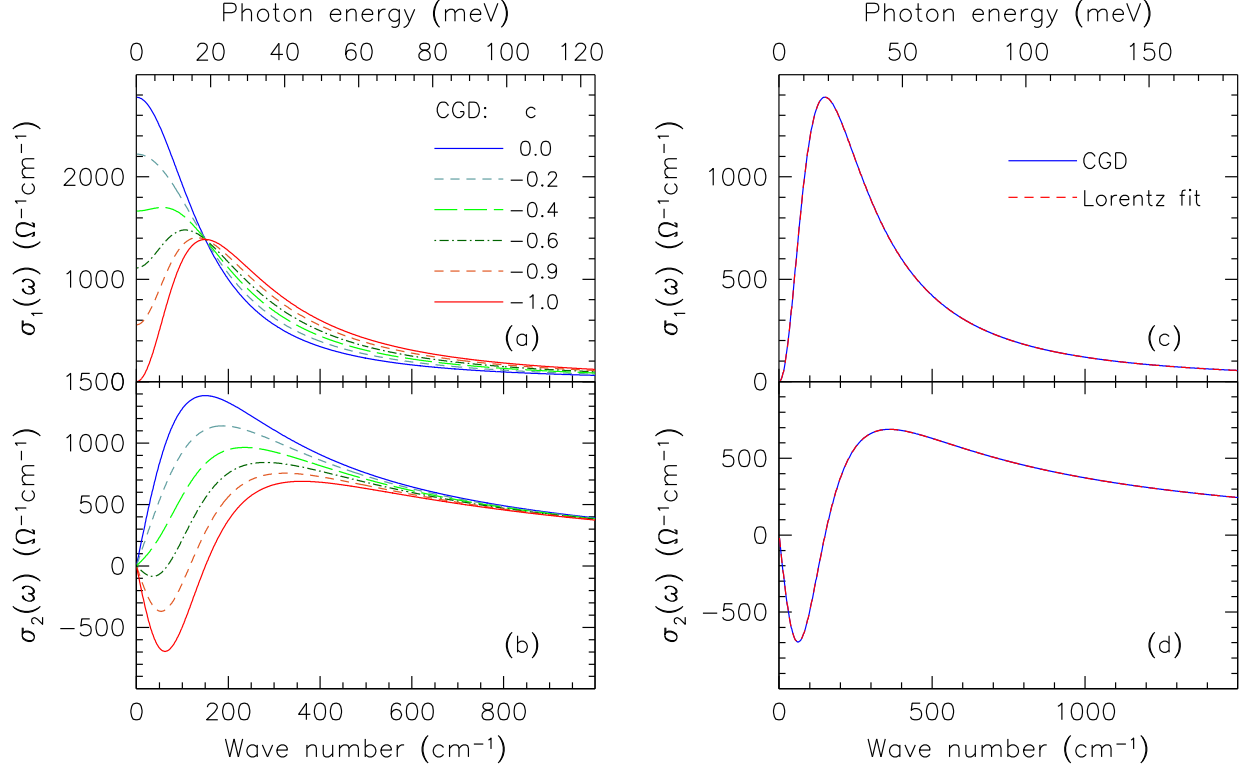


Figure S2. The (a) real and imaginary (b) parts of the optical conductivity for the classical generalization of the Drude model, using $\omega_p = 5000 \text{ cm}^{-1}$ and $1/\tau = 150 \text{ cm}^{-1}$, for several different values of c between 0 and -1 . The results of the Drude-Lorentz fit to the (c) real and (d) imaginary parts of the optical conductivity for $c = -1$, demonstrating the full spectral weight of the free carriers has been transferred into a Lorentzian centered at $\omega\tau = 1$ with width $2/\tau$.

an abrupt upturn emerges in the reflectance when $T < T_c$, corresponding to the superconducting transition observed in the resistivity [Fig. 1(b)].

CLASSICAL GENERALIZATION OF THE DRUDE MODEL

The classical generalization of the Drude model in the single-scattering approximation yields a complex conductivity $\tilde{\sigma}(\omega) = \sigma_1(\omega) + i\sigma_2(\omega)$ [5],

$$\tilde{\sigma}(\omega) = \left(\frac{2\pi}{Z_0}\right) \frac{\omega_p^2 \tau}{1 - i\omega\tau} \left[1 + \frac{c}{1 - i\omega\tau}\right], \quad (\text{S1})$$

where $Z_0 = 377 \Omega$ is the impedance of free space, $\omega_p^2 = 4\pi n e^2 / m^*$ is the square of the plasma frequency, with carrier concentration n and effective mass m^* , τ is the scattering time, and c represents the fraction of the carriers velocity that is retained after a collision. This model has particularly interesting values for $0 \geq c \geq -1$. For $c = 0$, a simple Drude model is recovered; however, increasingly localized behavior is observed as $c \rightarrow -1$. The classical generalization of the Drude model has been used to calculate the real and imaginary parts of the optical conductivity, shown in Figs. S2(a) and S2(b), respectively, using $\omega_p = 5000 \text{ cm}^{-1}$ and $1/\tau = 150 \text{ cm}^{-1}$, for several values of c between 0 and -1 . In Fig. S2(a) for $c \simeq -0.4$, a shoulder has developed in the real part of the optical conductivity at [5]

$$(\omega\tau)^2 = \frac{3c + 1}{c - 1}. \quad (\text{S2})$$

For $c = -1$, $\sigma_1(\omega \rightarrow 0) = 0$ and the carriers are now completely localized with a peak at $\omega\tau = 1$, or 150 cm^{-1} .

To demonstrate that the conductivity at $c = -1$ is indeed a Lorentzian which has captured all of the free-carrier spectral weight, we have fit the real and imaginary parts of the optical conductivity using a Drude-Lorentz model using

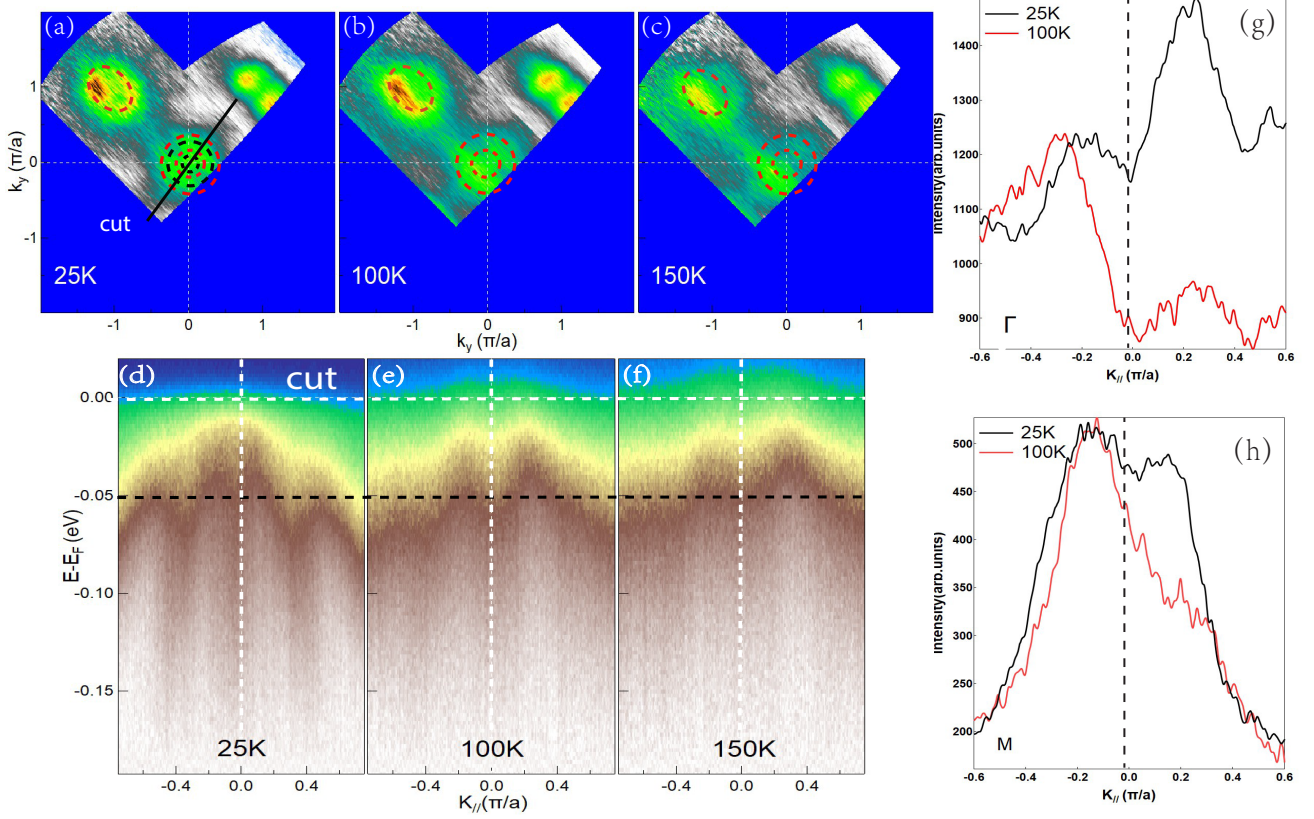


Figure S3. ARPES Fermi surface maps and $E - k$ cuts at 25, 100 and 150 K. (a–c) Fermi surface maps for optimally-doped Ca 10-3-8 at 25, 100 and 150 K, respectively. The dashed lines serve as a guide to the eye for the Fermi surface topology; the red dashed lines denote the hole pockets at 100 and 150 K, which are also shown at 25 K to allow for easier comparison. (d–f) The energy bands measured along symmetry cuts as shown in (a) by black line; (g) and (h) show the momentum distribution curves (MDCs) of hole-like bands around the Γ point, and the electron-like bands around M point measured at 50 meV below the Fermi energy [the black dashed lines in (d–f)]. The peak position corresponds to the bands position.

a non-linear least-squares technique, shown in Figs. S2(c) and S2(d), respectively. The fit returns a Drude component with no observable strength, and a single Lorentz oscillator centered at $\omega_1 = 150 \text{ cm}^{-1}$, with width $\gamma_1 = 300 \text{ cm}^{-1}$, and strength $\Omega_1 = 5000 \text{ cm}^{-1}$. (We also note that the fit returns $\epsilon_\infty = 1$). This clearly demonstrates that for $c = -1$ all of the spectral weight associated with the free carriers has been transferred to a localized excitation that is perfectly described by a Lorentzian oscillator.

ANGLE RESOLVED PHOTOEMISSION SPECTROSCOPY

Angle-resolved photoemission spectroscopy (ARPES) measurements have been performed to reveal how the electron and hole pockets evolve with temperature. The measurements were performed using a Helium lamp. The overall energy resolution was 10 meV for Fermi surface mapping and 4 meV for the cuts; the angular resolution was $\sim 0.1^\circ$. All the samples were measured in ultrahigh vacuum with a base pressure better than 5×10^{-11} mbar. The samples for temperature-dependent experiments were cleaved *in situ* at 20 K and measured at temperatures of 25, 100 and 150 K.

The Fermi surface of optimally-doped Ca 10-3-8 consists of two hole pockets around the Γ point (0,0) and one electron pocket around the M point (π, π). From the Fermi surface maps at 25, 100 and 150 K [Figs. S3(a–c), respectively], the Fermi surface topology shows little temperature dependence above 100 K, while an obvious decrease in the size of the hole pocket around Γ point may be seen at 25 K; the size of electron pocket remains constant at all measured temperatures. Figs. S3(d–f) show the $E - k$ cuts of the hole pockets; around the Γ point, a renormalization of the hole-like band may be seen just at 25 K. Comparing the momentum-distribution curves (MDCs) [Figs. S3(g) and (h)] made at 50 meV below Fermi energy [indicated by the black dashed lines in Figs. S3(d–f)], the decrease

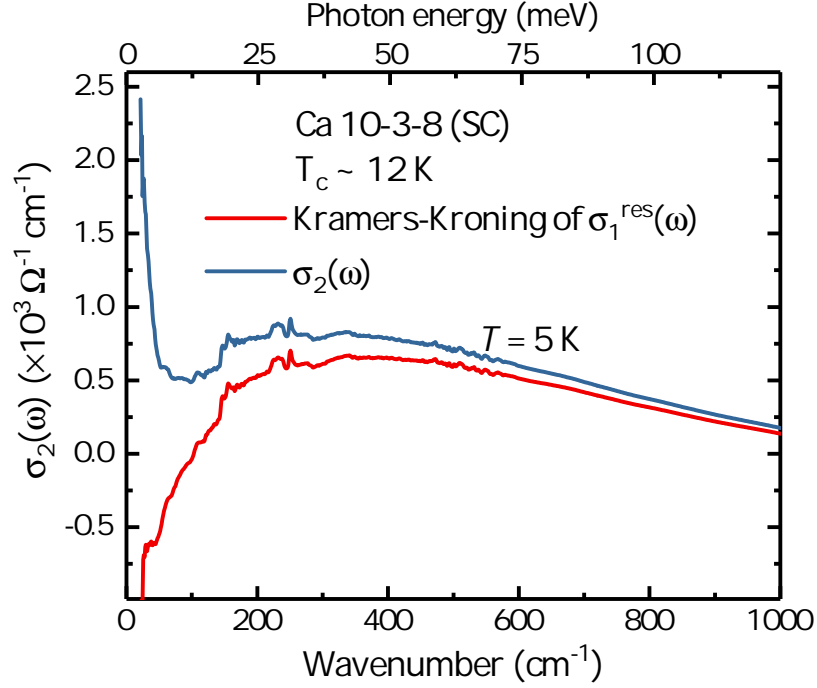


Figure S4. The blue curve is the imaginary part of the optical conductivity of the optimally-doped Ca 10-3-8 sample in the superconducting state ($\simeq 5$ K); the imaginary part of the conductivity calculated from the real part of the finite-frequency residual conductivity, $\sigma_1^{res}(\omega)$, is shown by the red curve.

in size of the hole bands may be observed, while the electron bands show no change below 100 K. The ARPES results are consistent with our optical spectroscopy measurements and temperature-dependent Hall coefficient [6], indicating a suppressed hole concentration. In addition, in Fig. S3(g), the narrowing of the MDC peaks at 25 K can further exclude the impurity scattering mechanism as the origin of the semiconducting-like behavior. In the optical conductivity, even though the low-energy intraband response is strongly suppressed below 100 K, none of the pockets detected by ARPES vanish, indicating that the multiband nature of Ca 10-3-8 is preserved.

DETERMINATION OF THE SUPERFLUID RESPONSE

The superfluid plasma can also be estimated from the imaginary part of the optical conductivity [7, 8]. In the superconducting state the real part of the optical conductivity may be expressed as:

$$\sigma_1(\omega) = \frac{\pi^2}{Z_0} \omega_{ps}^2 \delta(0) + \sigma_1^{res}(\omega), \quad (\text{S3})$$

in which $\sigma_1^{res}(\omega)$ is the conductivity, which does not contribute to the superfluid. The Kramers-Kronig transform of Eq. (S3) yields the imaginary part of the optical conductivity:

$$\sigma_2(\omega) = \frac{2\pi}{Z_0\omega} \omega_{ps}^2 - \frac{2\omega}{\pi} \int_0^\infty \frac{\sigma_1^{res}(\omega')}{\omega'^2 - \omega^2} d\omega'. \quad (\text{S4})$$

The imaginary part of the optical conductivity, $\sigma_2(\omega)$, may be calculated directly from the Kramers-Kronig analysis of the reflectivity $R(\omega)$. The second term of Eq. (S4) may be calculated from the residual conductivity $\sigma_1^{res}(\omega)$, which is simply the real part of the finite-frequency conductivity in the superconducting state. In Fig. S4 we show the imaginary part of the optical conductivity $\sigma_2(\omega)$ and the imaginary part of the conductivity calculated from $\sigma_1^{res}(\omega)$; the difference between these two curves is $2\pi\omega_{ps}^2/(Z_0\omega)$.

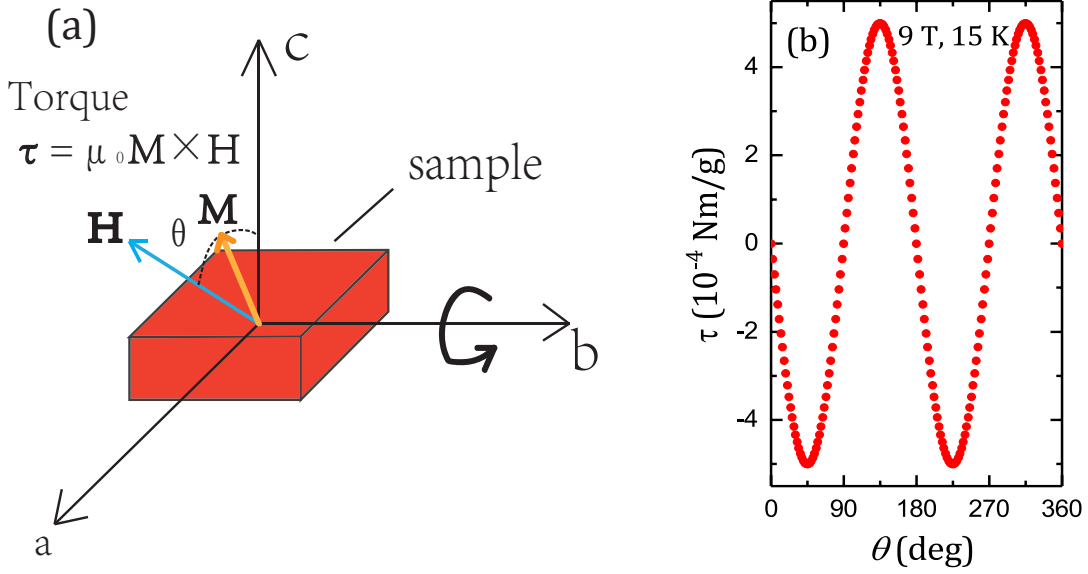


Figure S5. (a) The schematic representation of the experimental configuration. (b) The magnetic torque τ as a function of θ .

MAGNETIC TORQUE

The magnetic torque was measured as a function of angle and magnetic field over a wide temperature range by using a piezoresistive magnetometry. In piezoresistive magnetometry, the torque lever chip, together with a puck, is mounted on a PPMS horizontal rotator. The sample is mounted on the center of the chip using Apiezon N grease. A Wheatstone bridge circuit (integrated on the chip) detects the change in the resistance of the piezoresistors, produced by the changing magnetic torque [9]. During the measurement, the sample rotates around b axis, so that magnetic field \mathbf{H} is located in the a - c plane, as shown in Fig. S5(a). With this method, we can eliminate the isotropic Curie contribution due to impurity spins [10].

The magnetic torque is defined as $\tau(T, H, \theta) = \frac{1}{2}(\chi_c - \chi_{ab})H^2 \sin 2\theta$, in which χ_c is the magnetic susceptibility with the magnetic field $H \parallel \hat{c}$ and χ_{ab} , $H \perp \hat{c}$, θ is the angle between \mathbf{H} and c axis [as shown in Fig. S5(a)]. Therefore, $\tau_0 = \frac{1}{2}(\chi_c - \chi_{ab})H^2$ reflects the susceptibility anisotropy of Ca 10-3-8 [9, 11, 12]. The θ -dependent magnetic torque is shown in Fig. S5(b).

* xgqiu@iphy.ac.cn

† homes@bnl.gov

- [1] N. Ni, W. E. Straszheim, D. J. Williams, M. A. Tanatar, R. Prozorov, E. D. Bauer, F. Ronning, J. D. Thompson, and R. J. Cava, "Transport and thermodynamic properties of $(\text{Ca}_{1-x}\text{La}_x\text{FeAs})_{10}\text{Pt}_3\text{As}_8$," *Phys. Rev. B* **87**, 060507(R) (2013).
- [2] Christopher C. Homes, M. Reedyk, D. A. Crandles, and T. Timusk, "Technique for measuring the reflectance of irregular, submillimeter-sized samples," *Appl. Opt.* **32**, 2976–2983 (1993).
- [3] M. Dressel and G. Grüner, *Electrodynamics of Solids* (Cambridge University Press, Cambridge, 2001).
- [4] F. Wooten, *Optical Properties of Solids* (Academic Press, New York, 1972) pp. 244–250.
- [5] N. V. Smith, "Classical generalization of the Drude formula for the optical conductivity," *Phys. Rev. B* **64**, 155106 (2001).
- [6] N. Ni, J. M. Allred, B. C. Chan, and R. J. Cava, "High T_c electron doped $\text{Ca}_{10}(\text{Pt}_3\text{As}_8)(\text{Fe}_2\text{As}_2)_5$ and $\text{Ca}_{10}(\text{Pt}_4\text{As}_8)(\text{Fe}_2\text{As}_2)_5$ superconductors with skutterudite intermediary layers," *PNAS* **108**, E1019–E1026 (2011).
- [7] S. V. Dordevic, E. J. Singley, D. N. Basov, Seiki Komiya, Yoichi Ando, E. Bucher, C. C. Homes, and M. Strongin, "Global trends in the interplane penetration depth of layered superconductors," *Phys. Rev. B* **65**, 134511 (2002).
- [8] Y. M. Dai, H. Miao, L. Y. Xing, X. C. Wang, P. S. Wang, H. Xiao, T. Qian, P. Richard, X. G. Qiu, W. Yu, C. Q. Jin, Z. Wang, P. D. Johnson, C. C. Homes, and H. Ding, "Spin-Fluctuation-Induced Non-Fermi-Liquid Behavior with Suppressed Superconductivity in $\text{LiFe}_{1-x}\text{Co}_x\text{As}$," *Phys. Rev. X* **5**, 031035 (2015).
- [9] W. Zhang, K. Nadeem, H. Xiao, R. Yang, B. Xu, H. Yang, and X. G. Qiu, "Spin-flop transition and magnetic phase diagram in CaCo_2As_2 revealed by torque measurements," *Phys. Rev. B* **92**, 144416 (2015).
- [10] S. Kasahara, T. Yamashita, A. Shi, R. Kobayashi, Y. Shimoyama, T. Watashige, K. Ishida, T. Terashima, T. Wolf, F. Hardy,

- C. Meingast, H. v. Löhneysen, A. Levchenko, T. Shibauchi, and Y. Matsuda, “Giant superconducting fluctuations in the compensated semimetal FeSe at the BCS-BEC crossover,” *Nature Commun.* **7**, 12843 (2016).
- [11] H. Xiao, T. Hu, W. Zhang, Y. M. Dai, H. Q. Luo, H. H. Wen, C. C. Almasan, and X. G. Qiu, “Two distinct superconducting fluctuation diamagnetisms in $\text{Bi}_2\text{Sr}_{2-x}\text{La}_x\text{CuO}_{6+\delta}$,” *Phys. Rev. B* **90**, 214511 (2014).
- [12] Yayu Wang, Lu Li, M. J. Naughton, G. D. Gu, S. Uchida, and N. P. Ong, “Field-Enhanced Diamagnetism in the Pseudogap State of the Cuprate $\text{Bi}_2\text{Sr}_2\text{CaCu}_2\text{O}_{8+\delta}$ Superconductor in an Intense Magnetic Field,” *Phys. Rev. Lett.* **95**, 247002 (2005).